Observation of Mode-2 Internal Solitary Waves in the Northern South China Sea Based on Optical Remote Sensing

Zhixin Li, Jing Wang, Xu Chen, Kexiao Lu, Zhe Chang, Yage Lu, and Xiaochen Wang

***Abstract*—Due to the small scale and short lifetimes of mode-2 internal solitary waves (ISWs), they are seldom observed by satellite images. This study investigated the optical remote sensing imaging characteristics of mode-2 ISWs through physical simulation experiments, proposed a method for identifying mode-2 ISWs in optical remote sensing images, and conducted multisource optical remote sensing observation of mode-2 ISWs in the northern South China Sea (SCS). We have gathered over 10 000 images from seven optical remote sensing satellites, including Terra/Aqua, Gaofen-1/6, HJ-2A/B, and CBERS-04. A total of 342 mode-2 ISWs events were identified, exhibiting primary concentrations near Dongsha Atoll and the northern Heng–Chun Ridge in the northeastern SCS, as well as the Shenhu–Yitong Shoals in the northwestern SCS. Most mode-2 ISWs were observed within the 150–400 m water depth range along the continental shelf. The mode-2 ISWs primarily propagate in a northwestern direction, with propagation speeds approximately half that of the mode-1 ISWs. In the case of the northern Heng–Chun Ridge, mode-2 ISWs tended to propagate in a southwest direction. This study underscores the significant potential of high-resolution optical remote sensing satellites in observing mode-2 ISW and provides a new direction for studying mode-2 ISW.**

***Index Terms*—Mode-2 internal solitary waves (ISWs), multisource optical remote sensing, Northern South China Sea (NSCS), simulation experiment.**

I. Introduction

INTERNAL solitary waves (ISWs) are a common phenomenon in stratified oceans. They are widely distributed in marginal seas and continental shelf regions, where their propagation is accompanied by important energy transmission [1], [2], [3], [4]. Mode-1 ISWs affect marine processes such as sediment resuspension and ecosystem dynamics and threaten the safety of offshore engineering and underwater navigation, leading to a higher level of concern [5], [6], [7], [8], [9], [10], [11], [12]. The three-layer system of mode-2 ISWs displaces isopycnals in different directions in the upper and lower water columns [13], [14]. Many in-situ observations in recent years have underscored the widespread presence of mode-2 ISWs, suggesting their pivotal role in internal mixing phenomena within the oceanic environment [15], [16], [17], [18], [19], [20], [21]. Despite their relatively modest amplitudes and velocities compared with mode-1 ISWs, mode-2 ISWs engender flow shear approximately twice that of typical mode-1 counterparts, and mode-2 ISWs may have trapped core below the surface, posing a non-negligible threat to offshore platforms or underwater activities [22], [23]. The comprehension of the distribution and behavioral attributes of mode-2 ISWs is pivotal for coastal engineering endeavors and marine environmental monitoring initiatives. The South China Sea (SCS), one of the most frequently occurring sea areas for ISWs, holds records of different types and modes of ISWs [6], [24], [25]. The study indicates that the topographic features and favorable hydrological conditions in the northern South China Sea (NSCS) foster the emergence of mode-2 ISWs. These ISWs demonstrate a preference for an occurrence at a depth of 340 m, facilitating the efficient extraction of substantial energy from mode-1 ISWs [26]. Therefore, many undocumented mode-2 ISWs may exist in the NSCS.

Remote sensing presents novel avenues for the investigation of ISWs. Compared with expensive in-situ observations, optical remote sensing offers reduced data acquisition costs, and the combination of multisource optical remote sensing satellites facilitates continuous monitoring across a sea surface, allowing us to gain a more comprehensive understanding of the distribution, evolution, and characterization of ISWs [27], [28], [29], [30], [31], [32]. The interaction between wind-generated gravity-capillary waves and the surface current gradient induced by ISWs modulates the characteristics of surface short waves, thereby altering sea surface roughness and influencing the radiance observed by sensors through specular reflections of sunglint [33], [34], [35]. When the sensor is close to the direction of specular reflection, surface elements associated with smoother features (divergence regions) adhere to the geometric prerequisites of specular reflection, resulting in a bright stripe manifestation in optical remote sensing imagery. In comparison, surface elements associated with rougher features (convergence regions) manifest as dark stripes.

Manuscript received 8 February 2024; revised 22 May 2024; accepted 7 June 2024. Date of publication 14 June 2024; date of current version 1 July 2024. This work was supported by the National Natural Science Foundation of China under Grant 61871353. *(Corresponding author: Jing Wang.)*

Zhixin Li, Jing Wang, Zhe Chang, Yage Lu, and Xiaochen Wang are with the Department of Physics and Optoelectronic Engineering, Faculty of Information Science and Engineering, Ocean University of China, Qingdao 266700, China (e-mail: lizhixin_ouc@163.com; wjing@ouc.edu.cn; changzhe1845@stu.ouc.edu.cn; lyg7675@stu.ouc.edu.cn; wxc1278@stu.ouc.edu.cn).

Xu Chen and Kexiao Lu are with the Key Laboratory of Physical Oceanography, Ocean University of China, Qingdao 266005, China, and also with the Qingdao National Laboratory for Marine Science and Technology, Qingdao 266005, China (e-mail: chenxu001@ouc.edu.cn; lukexiao1234@163.com).

Digital Object Identifier 10.1109/JSTARS.2024.3414846

© 2024 The Authors. This work is licensed under a Creative Commons Attribution-NonCommercial-NoDerivatives 4.0 License. For more information, see https://creativecommons.org/licenses/by-nc-nd/4.0/

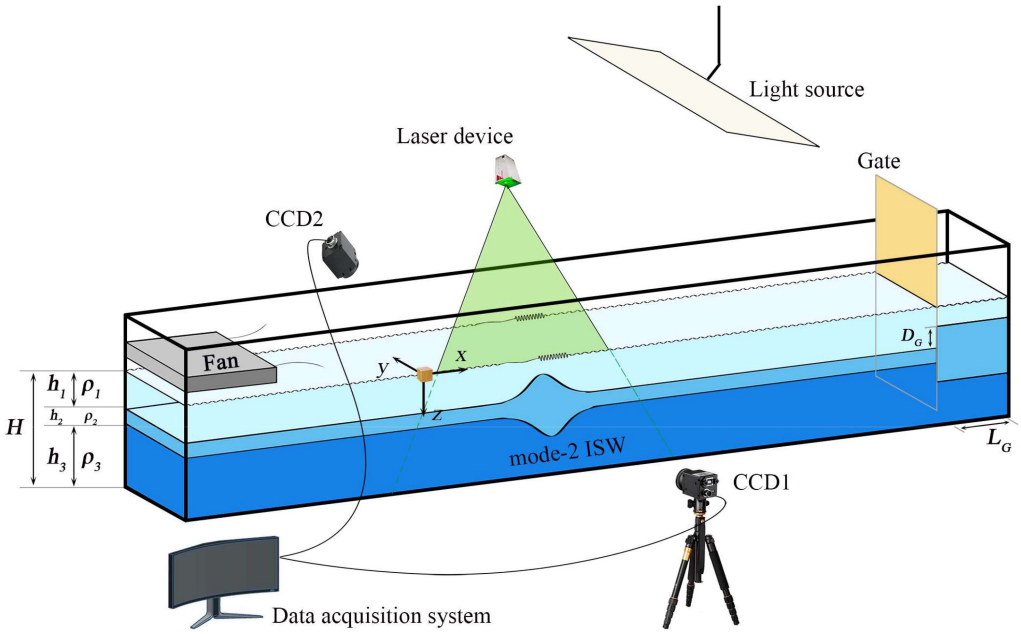

Fig. 1. Schematic diagram of the physical simulation experimental system.

Conversely, in areas devoid of sunglint, the order of bright-dark stripes is inverted [1], [36], [37]. Recent research indicates that ISW can not only alter the sea surface roughness but also induce Sea Surface Height Anomaly (SSHA), which can be observed by altimeters [5], [38], [39], [40]. Although the scale of mode-2 ISWs is small, physical simulation experiments have confirmed that they also produce free surface displacements (FSDs) at the water surface, which change the water surface slope and thus the reflection of light and play a role in optical remote sensing imaging [23].

Most mode-2 ISWs are small and limited by the spatial resolution of traditional optical remote sensing sensors, such as the Moderate Resolution Imaging Spectroradiometer (MODIS), which are often difficult to recognize in imagery. Consequently, their identification often necessitates validation via in-situ observations, phase speed analysis, or interpacket distance assessments [15], [41], [42]. Modern high-resolution optical satellites are more sensitive to sea surface variations, and the signals received by the sensors may be affected by a combination of vertical sea surface undulation and hydrodynamic modulation. To accurately recognize mode-2 ISWs in optical remote sensing images and extend the application of optical remote sensing in observing ISWs, it is necessary to study their optical remote sensing imaging characteristics deeply. The randomness of the generation of mode-2 ISWs makes it challenging to directly synchronize the analysis of mode-2 ISWs in terms of their sea surface manifestations and in-situ data. The physical simulation experiment provides the ideal controllable conditions to deal with these challenges and can promote the research of optical remote sensing imaging of ISWs [43], [44].

This article aims to explore the application of optical remote sensing satellites in observing mode-2 ISWs, including the study of optical remote sensing imaging characteristics of mode-2 ISWs based on physical simulation experiments and the observation and analysis of mode-2 ISWs in the NSCS based on multisource optical remote sensing. We have preliminarily studied the optical remote sensing imaging mechanism of mode-2 ISWs and clarified the identification method of mode-2 ISWs in optical remote sensing images. The mode-2 ISWs in the NSCS were observed using multisource optical remote sensing data, and their distribution characteristics and possible generation mechanisms were further analyzed.

II. Physical Simulation Experiment

A. Experimental Device and Method

The experiments were conducted in a gravity-stratified fluid flume with 300 × 15 × 30 cm dimensions. The physical simulation experimental system is shown in Fig. 1. In the Cartesian coordinate system, the horizontal direction is represented by x, the vertical direction parallel to the gravity acceleration vector is represented by z, and the y-axis is along the width of the flume. The origin is set at the leftmost water surface of the charge-coupled device-1 (CCD1) field of view. A planar light source replaces the radiation source, and a CCD2 is placed in the direction of its specular reflection. A horizontal square tube fan provides stable wind-generated surface waves on the water surface. A hand-held anemometer is utilized to obtain the wind speed at the sampling location, which varies to quantify the surface wave intensity R in the initial background.

Three layers of brine solutions with different densities were set up in the flume. The lower layer, with a density of 1.06 g/cm^3; is first added. Then the intermediate layer and upper layer, with a density of 1.04 g/cm^3; and 1.02 g/cm^3;, respectively, are gradually added using a floating sponge. This process forms a three-layer fluid characterized by double pycnoclines. The

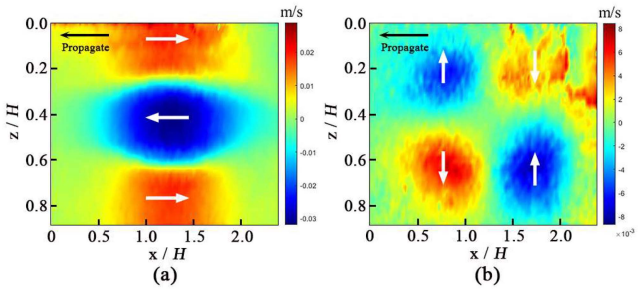

Fig. 2. Velocity field of mode-2 ISW. (a) Horizontal velocity field. (b) Vertical velocity field.

densities of the layers were labeled as ρ_1, ρ_2, and ρ_3, and their respective thicknesses were $h_1 = 6$ cm, $h_2 = 2$ cm, and $h_3 = 12$ cm.

A velocity measurement system based on particle image velocimetry (PIV) was used to visualize and quantify the velocity field of mode-2 ISWs in the xoz plane, which is implemented by laser, CCD1, and tracer particles. Polystyrene tracer particles with a diameter of about 50 μm and a density of about 1.04 g/cm^3 were uniformly dispersed in the flume. A laser emitting vertically downward is placed above the flume to illuminate the tracer particles in the vertical section. The movement of the tracer particles can be captured and recorded by the CCD1 as the ISW passes through the laser profile of the central part of the flume, and the velocity field of the two consecutive frames is calculated using the FFT-based cross-correlation algorithm. Taking the mode-2 ISW with a stable structure whose intermediate layer is located in the middle of the water column as an example, the horizontal and vertical velocity components of the mode-2 ISW are obtained, respectively (Fig. 2). Unlike the mode-1 ISW, the horizontal velocity field of the mode-2 ISW shows an apparent three-layer structure, with the current direction of the upper and lower layers being opposite to the propagation direction of the ISW and the current direction of the intermediate layer being the same as the propagation direction. There is also a distinct structural character to the vertical velocities, with an upward current ahead of the wave and a downward current behind the wave in the upper layer and the opposite in the lower layer. The vertical velocities are comparatively small and differ from the horizontal velocities by an order of magnitude.

ISW drives the horizontal surface current gradient, and in the framework of weak fluid interaction theory and Bragg scattering theory, the relationship between the remote sensing signature and the surface current gradient can be expressed as follows [27], [45]:

$$\frac{\Delta\sigma}{\sigma_0} \propto -\frac{\partial U}{\partial x} \tag{1}$$

where $\Delta\sigma = \sigma - \sigma_0$ denotes the deviation of the normalized radar cross-section σ from the mean value σ_0, U is the surface current velocity and x is the propagation direction of the ISW. The ISW-induced surface current has relatively rough surfaces at the convergence ($\partial U/\partial x < 0$) and relatively smooth surfaces at the divergence ($\partial U/\partial x > 0$). By measuring the horizontal current component of the xoz plane in the experiment, the variation of the surface current gradient with time in a given column can be solved.

ISW is generated by the gravity collapse of the stratified fluid. The step length and depth of the gravity collapse are L_G and D_G, respectively. A vertical gate is inserted at a distance of $L_G = 0.1\ m$ from the right wall of the flume. The brine solution with a density of ρ_2 is slowly injected into the intermediate layer of the wave-making region by a peristaltic pump, and the D_G of the upper/lower pycnocline on both sides of the gate is kept the same. The experiment was initiated by pumping off the gate vertically and smoothly, which resulted in the fluid collapsing on both sides of the gate and mode-2 ISW being generated in the intermediate layer and propagating into the central part of the flume. To avoid additional disturbances caused by complete pumping away from the gate, pump away until the bottom of the gate is flush with the water surface and place wave-absorbing sponges on the water surface in the vicinity of the gate to absorb surface disturbances with propagation speeds much higher than the ISW.

The fields of view of the two CCDs were calibrated to ensure that the spatial positions of the sampling lines were consistent in different viewing angles. The continuous images of the ISWs propagation process were acquired by the data acquisition system controlling the two CCDs simultaneously at 30 fps to ensure the consistency of the sampling time. Time-series processing is performed separately on the images acquired by the two CCDs to obtain the pixel values of a given column in the digitized image recorded by the camera over time. Here, we assume that the ISW is two-dimensional, i.e., uniform across the width of the flume, which is indeed the case from experimental observations.

B. Experimental Phenomenon

The relative azimuth angle of CCD1 to the light source is 180°, the zenith angle is 20°, and the gravity collapse step L_G and depth D_G remain unchanged. The experiments were set up with five different initial backgrounds of the water surface, and the surface wave intensities R_1-R_5 corresponded to the five experiments E1-E5. R_1 is the windless and calm water surface, and R_5 is the maximum value of the experiments that ensure the simulated optical remote sensing imaging and the simultaneous acquisition of the velocity field.

The initial background was determined based on the water surface in the 15 s preceding the experiment, as illustrated in Fig. 3(a)–(c). The profiles give the course of the grayscale values received by CCD2 over time [Fig. 3(d)–(f)]. When no wind is applied [Fig. 3(a)], there is no initial wind-generated surface wave, the water surface remains calm, and the grayscale is relatively stable [Fig. 3(d)]. A horizontal square tube fan near the water surface induced a steady wind, leading to fluctuations at the surface sampling location, as observed and recorded by CCD2. The resulting time series plot displays vertical stripes [Fig. 3(b)], and the profile also shows an expanded range of grayscale value variations [Fig. 3(e)]. As the wind speed increases, the uniformly distributed high-frequency surface waves

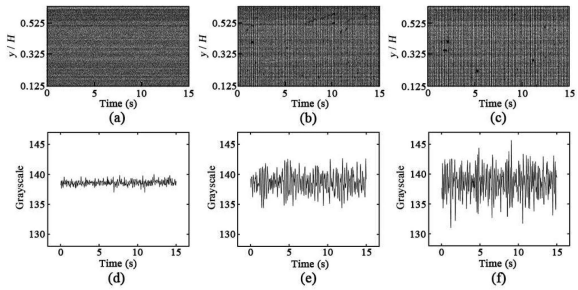

Fig. 3. Initial background of the water surface. (a) E1 with no initial surface waves. (b) Moderate intensity surface waves in E3. (c) High-intensity surface waves in E5. (d)–(f) Corresponding grayscale profiles.

in the background become more pronounced, while the range of grayscale values is further expanded [Fig. 3(c) and (f)].

The mode-2 ISW was generated and propagated in the intermediate layer, as shown in Fig. 4, where the changes in the waveform of the ISW and the simulated optical remote sensing image are visible. Fig. 4(a) shows a typical mode-2 ISW (E3), displayed using a pseudo-colour scheme. The FSD generated by the ISW on the water surface can be viewed as a soliton-like wave, having a similar scale to the ISW and accompanying its propagation, which can be approximated by a square hyperbolic secant function [23], [46], [47]. We visualized the FSD in the three-dimensional modeling software Solidworks using functional expressions based on the experimental parameters, as shown in Fig. 4(b). Considering that the FSD is tiny and cannot be visualized, we have magnified the schematic to demonstrate its features better.

Fig. 4(c) shows the simulated optical remote sensing image of the ISW, and the blue dashed rectangular box on the left shows the stable surface waves at the sampling location before the ISW arrives. As the ISW passes by (yellow dashed rectangular box), the surface waves above the wave's leading side are stretched, decreasing the surface roughness and showing brighter stripes in the image than the background. Surface waves converge above the trailing side of the wave, increasing surface roughness and making the corresponding region darker. Fig. 4(d) records the grayscale profile acquired by the CCD2, confirming that the mode-2 ISW exhibits bright-dark stripes, where the relative grayscale is the ratio of grayscale to the background in the simulated optical remote sensing image of the ISW. The time difference between the extreme points of the grayscale profile is T_{p-p}.

Fig. 4(e) records the change of surface current gradient with time at the same sampling position, and its trend is similar to that of the simulated optical remote sensing signal of ISW. As the ISW passes, the surface current gradient gradually increases, then decreases to a negative value. The time difference between the extreme points of $\partial U/\partial x$ is T_d, representing the time interval of the maximum value of convergence/divergence produced by the surface current.

T_{p-p} in the grayscale profile and T_d in the surface current gradient profile can be calculated in the following equations:

$$T_{p-p} = \frac{\Delta_{p-p}}{C_{fps}} \tag{2}$$

$$T_d = \frac{\Delta_d}{C_{fps}} \tag{3}$$

where Δ_{p-p} and Δ_d represent the pixel difference between the extreme points in the grayscale profile and the surface current gradient profile, respectively, and C_{fps} is the acquisition frame rate of the camera.

The peak-to-peak (p-p) distance is an essential parameter for ISW in optical remote sensing images, denoting the p-p distance in the simulated optical remote sensing images as D_{p-p} and in the surface current gradient profile as D_d

$$D_{p-p} = T_{p-p} \cdot v \tag{4}$$

$$D_d = T_d \cdot v \tag{5}$$

where v is the propagation speed of the ISW.

It should be noted that although we did not apply the initial wind-generated surface waves to E1, the upper flow field of the ISW also generates some low-intensity fluctuations at the water surface, and the CCD2 captures these responses. Therefore, we should pay attention to its modulation of surface waves even when discussing ISW imaging of initially calm water.

C. Imaging Analysis

To explore the imaging characteristics of mode-2 ISW in simulated optical remote sensing images, we analyzed FSD and the hydrodynamic modulation of the surface wave by surface current gradient, respectively.

The FSD generated by the mode-2 ISW at the water surface is small, making it difficult to extract the waveform from the CCD1 directly. To visualize the change of the water surface when ISW passes by more intuitively, we interpolate the original signal into a denser grid and retrieve the grayscale value related to the water surface. The results show that in all five sets of experiments, we observed the presence of FSDs (Fig. 5), whose characteristic lengths approximate those of ISWs. Although FSD is very small, it still plays a role in the optical remote sensing imaging of ISW. The FSDs produced by E1–E5 are nearly identical due to the same stratification and gravity collapse conditions. Therefore, in our analyses, the FSD in all experiments will be considered to contribute equally to the simulated optical remote sensing imaging of ISW.

We note that when different surface wave intensities R are applied to the water surface, there is a difference between Δ_{p-p} obtained based on the simulated optical remote sensing image and Δ_d obtained based on the surface current gradient, as shown in Fig. 6(a). When the water surface is calm (E1), Δ_{p-p} and Δ_d significantly differ. The increase in Δ_{p-p} is observed with the increase of R, while Δ_d remains relatively stable, and the two values gradually approach each other numerically. This trend may arise due to the combined influence of FSD and the hydrodynamic modulation of surface waves by the surface current gradient on the simulated optical remote sensing imaging of ISW. With the change in surface wave intensity, the modulation effect of the surface current gradient also changes.

The ratio between D_{p-p} and D_d is used to evaluate the weight of the modulation effect of surface current gradient on the surface

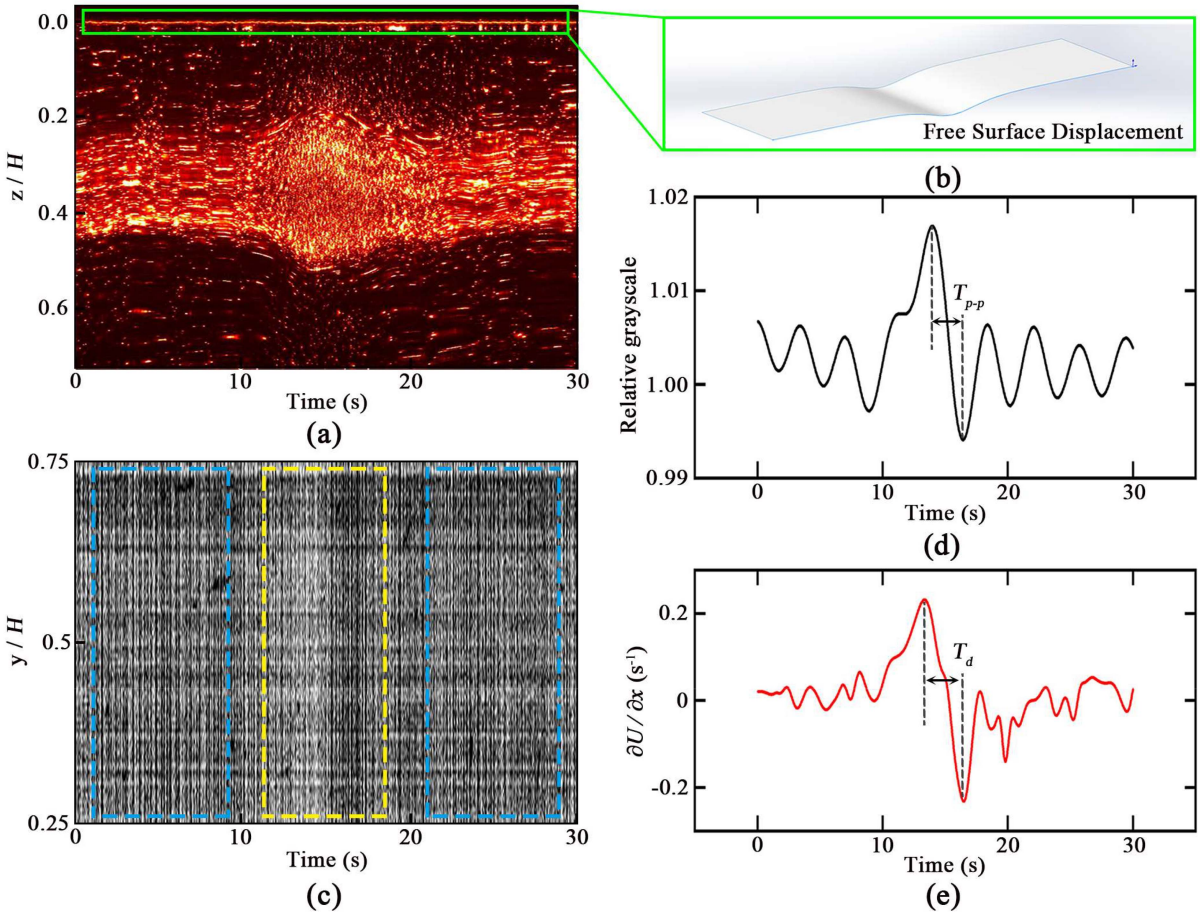

Fig. 4. Synchronous observation and calculation of simulated optical remote sensing imaging and surface current gradient of E3. (a) In-situ waveform diagram of mode-2 ISW. (b) Schematic diagram of FSD generated by ISW on the water surface. (c) Feature stripes of ISW in simulated optical remote sensing imaging. (d) Grayscale profile of simulated optical remote sensing image. (e) Surface current gradient profile of ISW.

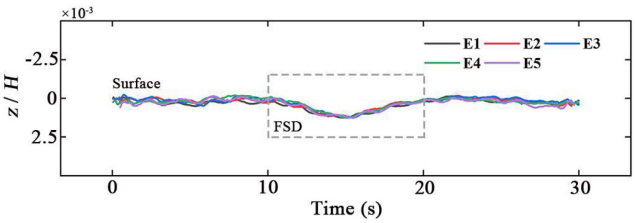

Fig. 5. FSD generated by mode-2 ISW on the water surface.

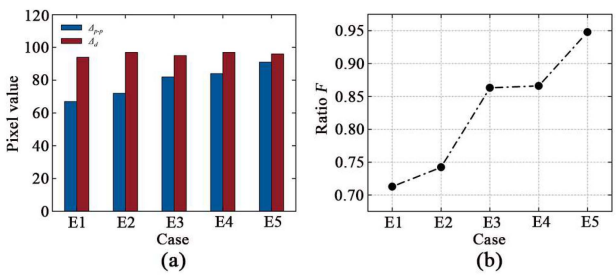

Fig. 6. (a) Δ_{p-p} in simulated optical remote sensing images and Δ_d based on surface current gradient. (b) Relationship between Δ_{p-p} and Δ_d.

wave in simulated optical remote sensing imaging

$$F = \frac{D_{p-p}}{D_d} \tag{6}$$

substituting (2)–(5) into (6)

$$F = \frac{\Delta_{p-p}}{\Delta_d}. \tag{7}$$

F is calculated according to Fig. 6(a), and as shown in Fig. 6(b), the D_{p-p} of ISW in the simulated optical remote sensing image cannot be fully explained by the modulation effect of the surface current gradient on the surface waves. When the water surface is calm, the F is only 0.71, and the influence of the tiny FSD in the water surface on the imaging can not be ignored. When surface waves are present in the initial background, the modulation of surface waves by the surface current gradient gradually dominates the imaging. The intensity of surface waves continues to increase within the scope of ensuring imaging. The position of the extreme point of bright/dark in the grayscale profile is almost the same as that of the extreme point of the surface current gradient induced by ISW on the water surface, indicating that the heterogeneity of surface roughness caused by the modulation of surface current gradient takes a significant

weight in the optical remote sensing imaging of ISW when the surface wave reaches a certain intensity.

Therefore, the imaging of mode-2 ISWs in optical remote sensing images is influenced by the FSD and the modulation of surface waves by the surface current gradient. When the sea surface is calm, the role of FSD is reflected in the optical remote sensing images. When some surface waves are present at the sea surface (the vast majority of the time), the optical remote sensing imaging characteristics of mode-2 ISWs may be more modulated by the upper flow field. In addition, Fig. 6(a) shows that there may be a relationship between p-p distance in the optical remote sensing images and the background of the sea surface. The p-p distance plays an essential role in the parameter inversion of ISWs [48], so the relationship between the two is worthy of further investigation.

III. Optical Remote Sensing Observation of Mode-2 ISWs

A. Image Interpretation of Mode-2 ISWs

The experimental results show that the effect of FSD on imaging is not negligible only when the sea surface is calm. In most cases, optical remote sensing imaging of mode-2 ISWs is dominated by their modulation of the upper flow field, and the bright stripe appears before the dark stripe in the sunglint area of the optical remote sensing image. The mode-2 ISWs and elevation mode-1 ISWs both exist on the continental shelf of the shallow sea and have similar imaging characteristics. Therefore, the interpretation of mode-2 ISWs in optical remote sensing images cannot only rely on the order of bright and dark stripes. The image's geometric angle, seawater stratification, and depression mode-1 ISWs near the stripes are essential for correctly interpreting mode-2 ISWs.

Two optical remote sensing images obtained on August 23 and October 21, 2021, provide a schematic view of the ISWs in the NSCS. Alternating bright and dark stripes associated with the ISWs can be recognized from the images [Fig. 7(a) and (g)]. Among them, Fig. 7(a) is located in the sunglint area of the MODIS image, the curvature of the wavefront indicates that the ISWs propagate to the northwest, and ISW1 and ISW2 show different sequences of bright and dark [Fig. 7(b) and (c)]. To identify the type of ISWs we observed, the radiance distribution along the propagation direction of the waves was measured using ENVI v.5.6 [Fig. 7(d) and (e)], which confirmed our initial visual judgment based on the images. The water depth was obtained using the General Bathymetric Chart of the Oceans (GEBCO-2023) with a resolution of 15 arc seconds. The Brunt–Väisälä frequency $N_{(z)}$ was calculated from climate stratification profiles provided by the 1/4° × 1/4° World Ocean Atlas 2018 (WOA18) downloaded from NOAA's National Ocean Data Center (NODC) website [Fig. 7(f)]. ISW1 and ISW2 are located in water depths of 332 m and 317 m, respectively, and the average depth of the upper layer in this area in August was 51 m, much less than the thickness of the lower layer. Therefore, the dark-bright stripes displayed by ISW1 are consistent with the interpretation of a depression mode-1 ISW. Considering that elevation mode-1 ISWs are typically observed in areas where

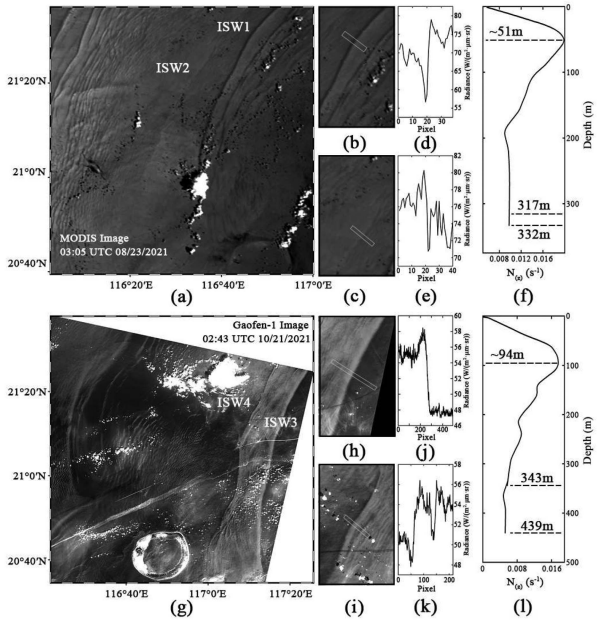

Fig. 7. ISWs in optical remote sensing images. (a) MODIS image of ISWs in the sunglint area obtained on August 23, 2021. (b) and (c) Magnified ISW and the corresponding radiance profiles in (d) and (e). (f) Profile of the Brunt–Väisälä frequency $N_{(z)}$ calculated from WOA18. (g) Gaofen-1 image of ISWs in the nonsunglint area obtained on October 21, 2021. (h) and (i) Magnified ISW and corresponding. (j) and (k) Radiance profiles. (l) Profile of the Brunt–Väisälä frequency $N_{(z)}$ calculated from WOA18.

the depth of the upper layer exceeds that of the lower layer, and given the presence of depression mode-1 ISWs northwest of ISW2 (in shallower areas), ISW2 can be considered a standard case of mode-2 ISWs.

Fig. 7(g) shows the image of the nonsunglint area of Gaofen-1 after enhanced display, with the presence of ISW3 and ISW4 characterized by clear stripes [Fig. 7(h) and (i)]. The order of bright and dark stripes of the ISWs is reversed due to the geometrical angle of the imaging of the nonsunglint area. Fig. 7(l) shows the local stratification, and although the pycnocline is located deeper, the thickness of the upper layer in this area is still smaller than that of the lower layer, and no elevation mode-1 ISWs should be present. Therefore, ISW4 with dark-bright stripes characteristics is also a typical mode-2 ISW.

In addition, in the area where the elevation mode-1 ISWs are widely distributed, such as within 100 m of water depth, we have not been able to determine the convex mode-2 ISWs from the monthly stratification unless the presence of well-characterized depression mode-1 ISWs in the vicinity is verified.

B. Mode-2 ISWs in the NSCS

MODIS is a crucial optical sensor onboard NASA's Terra/Aqua satellite, which has an image width of up to 2330 km and can provide images in discrete bands with resolutions of 250 m, 500 m, and 1000 m, respectively. The 250 m resolution band is commonly used in remote sensing studies of ISWs. The two satellites operate alternately, allowing two observations of the same area in one day. Gaofen-1 is the first satellite in China's

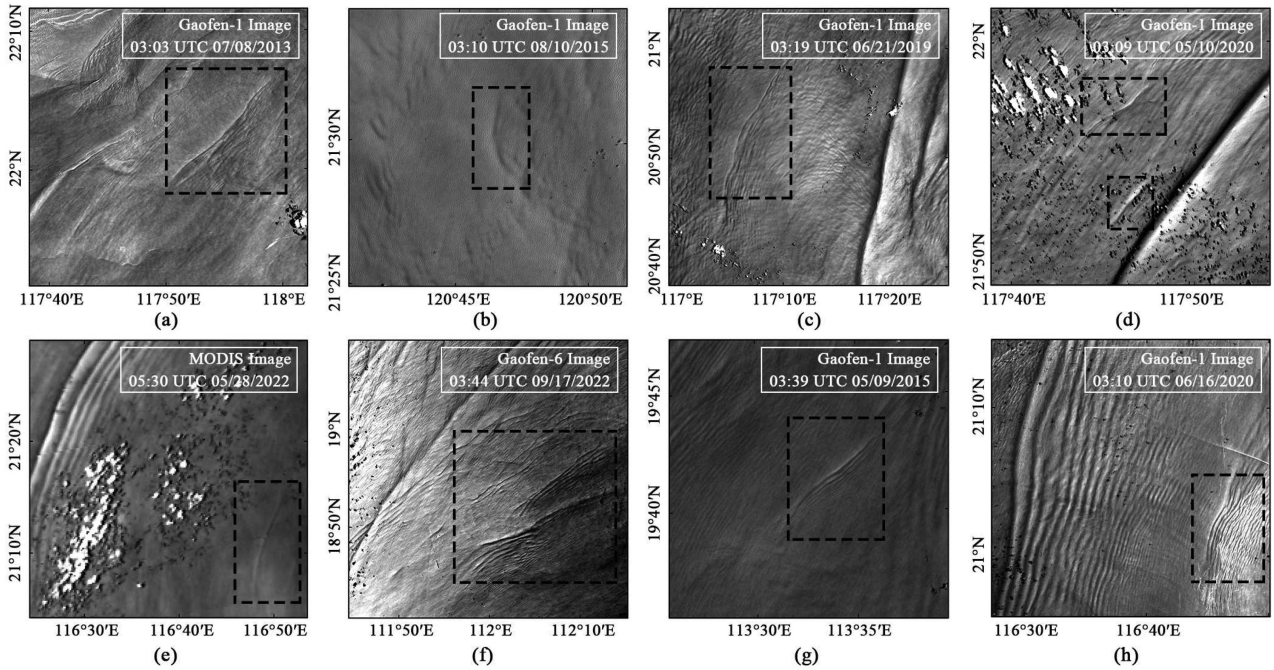

Fig. 8. Mode-2 ISWs are propagating as solitons or wave packets. (a)–(e) Mode-2 ISWs in the form of solitons in the NSCS. (f)–(h) Wave packets of mode-2 ISWs in the NSCS. The black dashed boxes are mode-2 ISWs.

high-resolution earth observation system, and it was officially launched in 2013. In 2019, Gaofen-6 was put into operation. Both satellites have a spatial resolution of 16 m and transit between 10:30 and 11:30 local time with a revisit period of only four days. HJ-2A/B is a pair of satellites developed by China to improve disaster monitoring and forecasting, they were launched in 2020 and equipped with multiple visible light CCD cameras with a spatial resolution of 16 m. Through splicing, 800 km wide multispectral images can be realized. CBERS-04 is an Earth resources satellite jointly developed by China and Brazil, carrying a PAN sensor that can provide images with a spatial resolution of 10 m. The high-resolution data obtained from Gaofen-1/6, HJ-2A/B, and CBERS-04 effectively compensate for the spatial resolution limitations in MODIS imagery, thereby addressing the problem of optical remote sensing observation of small-scale mode-2 ISWs. Through the cooperation of multisource satellites, the temporal resolution of remote sensing observation in the target sea area can reach one day. We observed a large number of mode 2 ISWs in the NSCS, a total of 342 events, using more than 10 000 views of optical remote sensing images from seven satellites, Gaofen-1 in 2013–2022, and Terra/Aqua, HJ-2A/B, Gaofen-6, and CBERS-04 in 2020–2022. As shown in Fig. 8, they tend to have similar basic characteristics, primarily manifesting as solitons, with only a minority exhibiting characteristics akin to wave packets. In Areas I and III, they are often accompanied by mode-1 ISWs. We also find that most of these ISWs with clear surface manifestations appear in May-September. This seasonal variation could be attributed to the stratification in the NSCS, where the pycnocline is shallower in summer and the upper flow field is closer to the water surface, resulting in more distinct bright and dark stripes in the sunglint area of optical remote sensing images.

The images containing mode-2 ISWs were orthorectified and image enhanced in ENVI v5.6, and the wavefronts of the leading waves were extracted using the function of regions of interest (ROI). Their geographic locations were digitized and displayed on a diagram of the NSCS (Fig. 9). It can be seen that the mode-2 ISWs of the NSCS are mainly concentrated in three active areas. They are located in the Dongsha Atoll (Area I) and the northern Heng–Chun Ridge (Area II) in the northeastern SCS, as well as the Shenhu–Yitong Shoals (Area III) in the northwestern SCS. In particular, the northeastern Dongsha Atoll contains the most densely distributed occurrences of these phenomena. Notably, Area III is the first time mode-2 ISWs have been observed, which may have yet to be noticed in previous studies. Unlike the widely distributed mode-1 ISWs in the NSCS, mode-2 ISWs are distributed in a more concentrated depth range. They are regularly distributed at depths of 150–400 m in Areas I and III, and almost all of the mode-2 ISWs in Area II are distributed in the channel between the Heng–Chun Ridge and southern Taiwan Island. Mode-2 ISWs in Area I propagate predominantly to the west or northwest, those in Area II propagate predominantly to the southwest, and those in Area III almost always propagate to the northwest. The wavefront is nearly parallel to the local isobath in all areas, indicating that the wave propagation direction is essentially perpendicular to the isobath.

The wavefront lengths of the leading waves of mode-2 ISWs in the NSCS were counted, as shown in Fig. 10(a). The average wavefront length of mode-2 ISWs in the three areas is 13.49 km, with more than 80% of the waves having a wavefront length of less than 20 km—only 20% of the average wavefront length

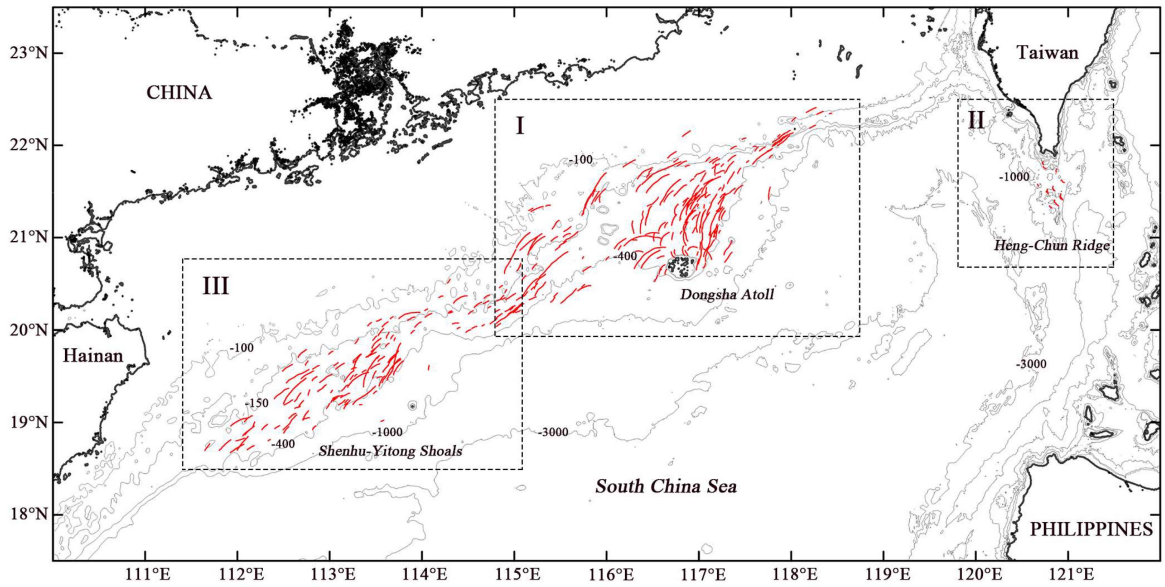

Fig. 9. Distribution of mode-2 ISWs in the NSCS. The red curve shows the mode-2 ISWs observed in optical remote sensing images. The black dotted line frame shows the active area of mode-2 ISWs. The shallower lines are isobath, measured in meters.

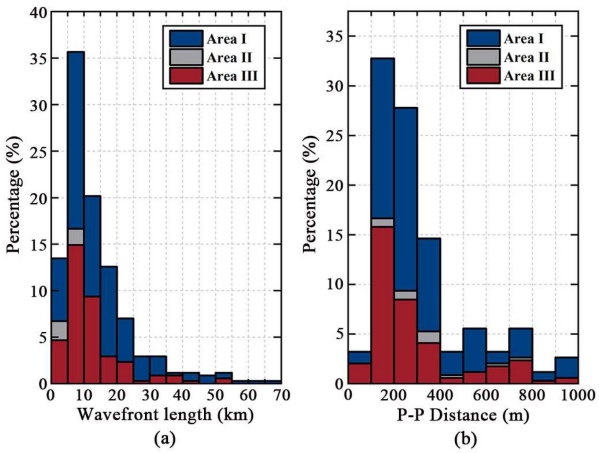

Fig. 10. Characteristic parameters of mode-2 ISWs in the NSCS. (a) Wavefront length (km). (b) p-p distance (m).

of mode-1 ISWs [31]. In Area I, the average wavefront length is 14.83 km, and the scale of ISWs in this area is diverse, especially since the wavefront length of large-scale mode-2 ISW is comparable to that of mode-1 ISW. A few mode-2 ISWs were captured in Area II, with an average wavefront length of 5.37 km. The average wavefront length of mode-2 ISWs in Area III is 12.19 km, similar to that in Area I. Fig. 10(b) illustrates the p-p distances of mode-2 ISWs, showing an average p-p distance of only 313 m. Approximately 80% of these mode-2 ISWs exhibit p-p distances between 100 and 400 m. In addition, mode-2 ISWs with large p-p distances were observed in Area I.

IV. Discussion

In this study, the multisource optical remote sensing satellites were used to observe the mode-2 ISWs in the NSCS for the first time, and their spatial distribution and remote sensing characteristics were obtained. From Fig. 9, most mode-2 ISWs have straight wavefronts or only a tiny convex curvature. It can be assumed that these waves were generated in a relatively short time before the acquisition of the optical remote sensing images and have short lifetimes (if they have long lifetimes, the wavefronts are more likely to have convex curvature) [49]. Unlike mode-1 ISWs, mode-2 ISWs are more dispersive and may propagate and evolve as solitary waves over the continental shelf for only a short time [50]. However, further discussion of their possible generation mechanisms and propagation characteristics in the three active areas mentioned earlier is still warranted.

A. Dongsha Atoll

The mode-2 ISWs in Area I are mainly concentrated in the northeast of Dongsha Atoll, and the other part is distributed along the 150 m isobath in the northwest. During the summer, it can be observed that mode-2 ISWs located on the slope of the shelf followed mode-1 ISWs, as shown in Fig. 11. This phenomenon is consistent with the results of Yang et al. [15], who believed that this may be attributed to the shoaling process of mode-1 ISWs or internal tides (ITs). Qian et al. [41] used the Massachusetts Institute of Technology Generalized Cyclic Model (MITgcm) to study the evolution of the shoaling of depression mode-1 ISWs in the area, and the results of numerical simulations showed that mode-2 ISWs are generated by the interaction of mode-1 ISWs with upslope topography.

Multiple mechanisms may sometimes coincide in the same area [15], [18], [26], [50].

Multisource satellite images can be used to jointly observe the propagation of the same ISW within a specific time window, and the propagation speed of the ISW can be estimated by the geolocation of the wavefront and the time difference between image pairs, which is referred to as the multitemporal image

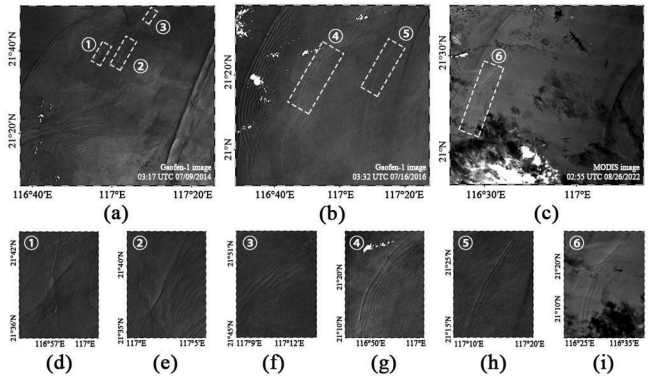

Fig. 11. Optical remote sensing images of mode-2 ISWs following mode-1 ISWs in the northern Dongsha Atoll. (a) and (b) Gaofen-1 images acquired on July 9, 2014, at 03:17 UTC and July 16, 2016, at 03:32 UTC, respectively. (c) MODIS image acquired on August 26, 2022, at 02:55 UTC. (d)–(i) Zoomed-in images of the mode-2 ISWs framed by white rectangles.

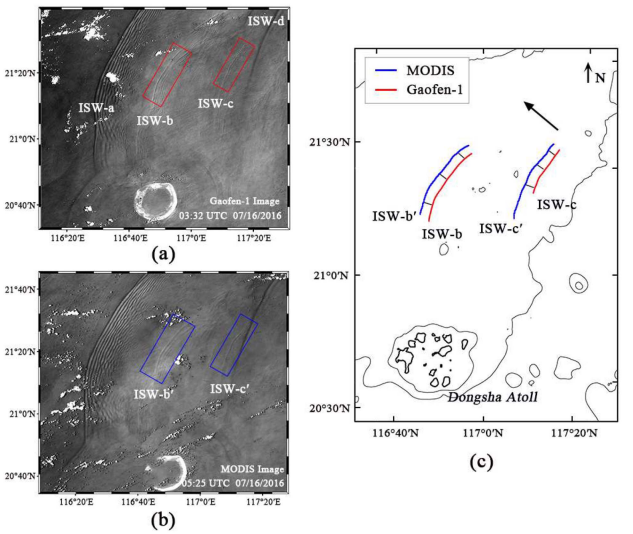

Fig. 12. Estimating the propagation speed of mode-2 ISWs using the MTI method. (a) Gaofen-1 and (b) MODIS images obtained north of Dongsha Atoll on July 16, 2016, show the mode-2 ISWs appearing between the two mode-1 ISWs. (c) Wavefront projection of mode-2 ISWs. The red solid line is the ISWs in the Gaofen-1 image, the blue solid line is the ISWs in the MODIS-Aqua image, and the black arrow represents the direction of wave propagation.

(MTI) method [51]. We found mode-2 ISWs with distinct surface manifestations and convex curvature north of Dongsha Atoll (Fig. 12), which implies their amplitude may be larger than usual. Large-amplitude mode-2 ISWs have internal recirculation areas that enable long-range mass transport and relatively long lifetimes [52], allowing us to estimate their propagation speeds using the MTI method. For example, Gaofen-1 captured four ISWs on July 16, 2016 [Fig. 12(a)], where ISW-a and ISW-d are the mode-1 ISWs refracted by the Dongsha Atoll and the incident mode-1 ISWs in the next tidal period, respectively, and the surface manifestations in the image are dark-bright stripes. ISW-b and ISW-c, marked by red rectangular boxes, exhibit distinct bright-dark stripes, and the thickness of the upper layer of seawater at this location is smaller than the lower

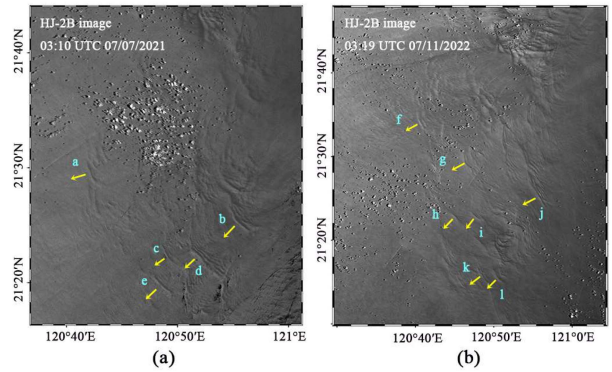

Fig. 13. HJ-2B images acquired in the northern Heng–Chun Ridge. (a) HJ-2B images acquired on July 7, 2021, at 03:10 UTC. (b) July 11, 2022, at 03:19 UTC show many mode-2 ISWs. Yellow arrows show the propagation direction of ISWs.

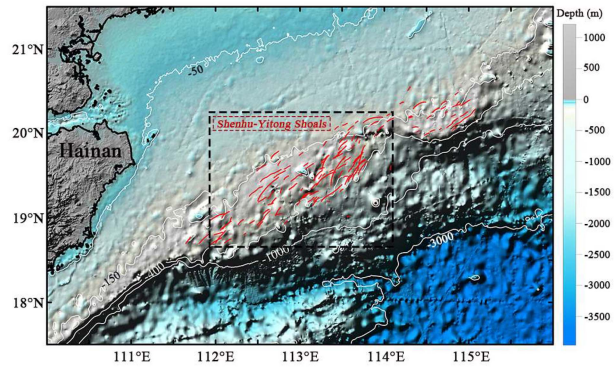

Fig. 14. Spatial distribution of mode-2 ISWs in Area III. The red curve is the mode-2 ISWs, the white solid line is the isobath, and the black dashed box is the distribution area of mode-1 ISWs obtained by Li et al. [56] using SAR, and the bottom terrain height is shown in the color bar.

layer so that they can be judged as typical mode-2 ISWs. After approximately two hours, MODIS-Aqua imagery captured the presence of the same ISWs denoted as ISW-b' and ISW-c', as depicted in Fig. 12(b), and highlighted with blue rectangular boxes. The mode-2 ISWs in the image pairs are georeferenced and wavefront projected in ArcGIS, as shown in Fig. 12(c). There is a navigational error of about half a pixel in the wavefront construction, and assuming a typical value of 0.60 m/s for the propagation speed of the mode-2 ISWs, the maximum error that can be incorporated into the speed estimation is about 3.09%. Similarly, the average propagation speed of mode-1 ISWs in Fig. 12 is estimated to be about 1.39 m/s using the MTI method, which aligns with previous research findings in the area [28]. Therefore, the propagation speed of mode-2 ISW is roughly half that of mode-1 ISWs.

B. Northern Heng–Chun Ridge

Early observations and theoretical studies indicate that the generating area of those "transbasin" waves reaching the continental shelf in the northeastern SCS is in the vicinity of the Bataan Islands in the Philippines, which are located on the

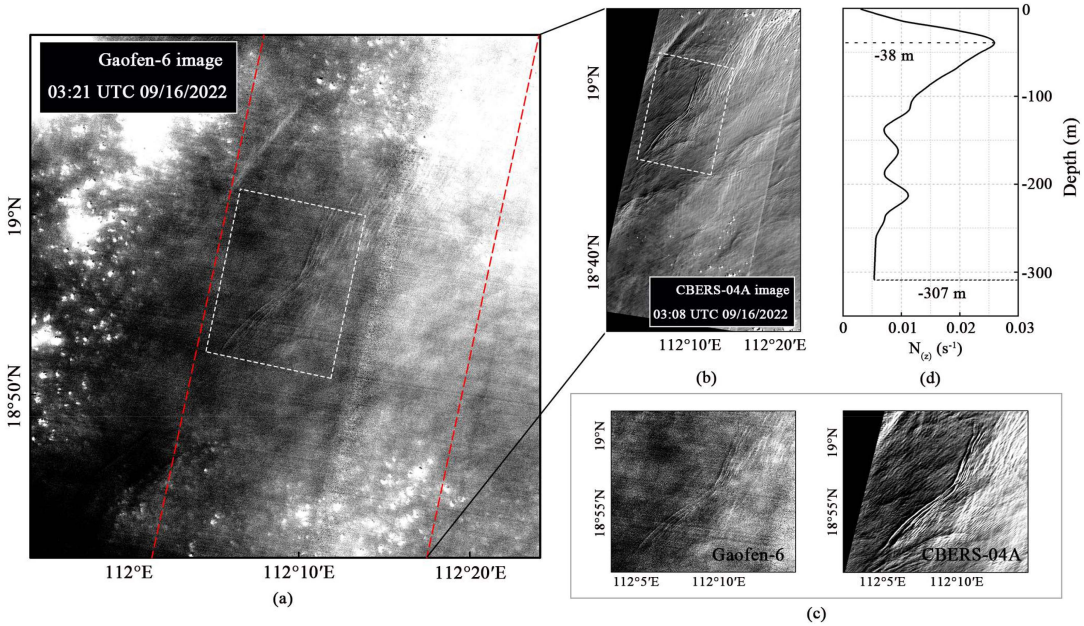

Fig. 15. Image pair acquired at Shenhu–Yitong Shoals. (a) Gaofen-6 image was acquired on September 16, 2022, at 03:21 UTC. (b) CBERS-04 image was acquired on September 16, 2022, at 03:08 UTC. (c) Mode-2 ISW in the image. (d) Profile of Brunt–Väisälä frequency $N_{(z)}$ calculated from WOA18. The red dotted box is the coverage area of the CBERS-04 image, and the white dotted box is the position of mode-2 ISWs.

eastern (Lan-Yu) ridge between Taiwan and the Philippines in the Luzon Strait [7]. Another theoretical study shows that some high-mode waves are often generated in the western (Heng–Chun) ridge (Area II in Fig. 9) [53]. Fig. 13 shows the HJ-2B image of the northern Heng–Chun Ridge. The image shows multiple stripes with prominent bright-dark characteristics. The yellow arrows represent the direction of wave propagation, and they almost all propagate southwestward. GEBCO-2023 shows that the water depth in this area is between 300 and 500 m, and the stratification cannot meet the conditions for elevation mode-1 ISWs. These stripes are considered to be the sea surface manifestations of mode-2 ISWs. The authors in [16] and [54] also carried out several cruises at the same location and observed mode-2 ISWs as solitons or wave packets. They found that the wave generation was consistent with local Lee wave dynamics. The length of the wavefront does not exceed 10 km due to the limitations imposed by the width of the channel and its proximity to the generating source. High-mode waves here propagate mainly in the northwest and southwest directions. Influenced by the eastward ebb tide, their propagation speeds are slower than the theoretical speeds computed from the climatic stratification data. Since the mode-2 ISWs here always dissipate within a few hours and do not propagate far outward [16], we did not find matching image pairs on the same day, but their positions and propagation directions are consistent with the observations of Ramp et al. [54].

C. Shenhu–Yitong Shoals

The northwestern SCS, located north of 15°N and west of Dongsha Atoll, consists of an extensive continental shelf, steep slopes, and many islands and shoals [55]. The Shenhu–Yitong Shoals (Area III) are between Hainan Island and Dongsha Atoll. Li et al. [56] used SAR images to obtain the distribution area of mode-1 ISWs at Shenhu–Yitong shoals (the range shown by the black dashed box in Fig. 14). They proposed that ITs generated in the Luzon Strait propagated westward into the SCS and met the continental shelf at Shenhu–Yitong shoals to evolve into ISWs. This view has been confirmed in recent studies [55]. The spatial distribution of mode-2 ISWs, as observed through multisource satellite data, exhibits an overlap with the geographical distribution of mode-1 ISWs as delineated by Li et al. [56]. Moreover, our statistical analysis shows that almost all mode-2 ISWs in this area appear behind mode-1 ISWs. Thus, it is plausible that these mode-2 ISWs are result from the interaction between mode-1 ISWs generated in this location and gently sloping terrain.

Mode-2 ISWs with long lifetimes characteristics are not found in Area III. Fortunately, we found a pair of ISWs with dark-bright stripes in the nonsunglint area of the two high-resolution optical remote sensing images obtained on September 16, 2022 [Fig. 15(a)–(c)]. The profile of the Brunt–Väisälä frequency $N_{(z)}$ calculated using WOA18 [Fig. 15(d)] confirms that the pair of stripes is a surface manifestation of mode-2 ISWs. Although the time interval between the two images was only 13 min, the superior spatial resolution of the satellite resulted in an error in speed estimates of only 1.75%, highlighting the advantages of the high-resolution optical satellite in observing mode-2 ISW. The average propagation speed of mode-2 ISWs estimated using MTI is 0.59 m/s.

V. Conclusion

Identifying and observing mode-2 ISWs in optical remote sensing images is an urgent problem that needs to be solved due to the limitation of traditional medium-resolution optical remote sensing satellites. This article explored the application

of optical remote sensing satellites in observing mode-2 ISWs. First, the imaging characteristics of mode-2 ISWs in optical remote sensing images were clarified based on physical simulation experiments. A comparative analysis of the characteristics of the optical remote sensing of mode-2 ISWs and the surface current gradient revealed that the optical remote sensing imaging of mode-2 ISWs in the laboratory was a superposition of the two characteristics of the FSD and the hydrodynamic modulation of the surface wave by the surface current gradient. When the water surface is calm, the FSD plays a part in imaging. When certain surface waves exist at the sea surface, the optical remote sensing imaging characteristics of mode-2 ISWs may be more modulated by the upper flow field. Based on the experimental results, the recognition method of mode-2 ISWs in optical remote sensing images was further proposed.

Second, we used multisource optical remote sensing satellites to observe mode-2 ISWs in the northern SCS and found that waves with clear surface manifestations mainly occur in May-September, which may be related to the stratification change of the NSCS in summer. Gaofen-1 images acquired from 2013 to 2022 and Terra/Aqua, HJ-2A/B, Gaofen-6, and CBERS-04 images acquired from 2020 to 2022 observed a total of 342 mode-2 ISWs in three main areas: the Dongsha Atoll and the northern Heng–Chun Ridge in the northeastern SCS, as well as the previously undocumented area of the Shenhu–Yitong Shoals in the northwestern area. Most mode-2 ISWs are in the 150–400 m range, distributed along the isobaths and propagating mainly to the northwest. The generation of mode-2 ISWs at the sloping shelf may be related to the interaction between mode-1 ISWs and topography, and the mode-2 ISWs at the northern Heng–Chun Ridge may be related to the Lee wave mechanism. At the same geographic location, the propagation speed of mode-2 ISW is usually only half that of mode-1 ISW.

The high-resolution optical remote sensing images show the capability of observing mode-2 ISW, and the synergy of multisource optical remote sensing satellites enables us to continuously observe the target sea area, which provides data security for further research on mode-2 ISW. Future work will focus on studying the propagation speed of mode-2 ISW in the NSCS, which will require more remote sensing data, and a combination of SAR and optical images will be a better choice.

REFERENCES

[1] B. Hu, J. Meng, L. Sun, and H. Zhang, "A study on brightness reversal of internal waves in the Celebes Sea using Himawari-8 images," *Remote Sens.*, vol. 13, no. 19, Oct. 2021, Art. no. 3831, doi: 10.3390/rs13193831.

[2] X. Zhang et al., "Oceanic internal wave amplitude retrieval from satellite images based on a data-driven transfer learning model," *Remote Sens. Environ.*, vol. 272, Apr. 2022, Art. no. 112940, doi: 10.1016/j.rse.2022.112940.

[3] S. Zhang, X. Li, and X. Zhang, "Internal wave signature extraction from SAR and optical satellite imagery based on deep learning," *IEEE Trans. Geosci. Remote Sens.*, vol. 61, Mar. 2023, Art. no. 4203216, doi: 10.1109/TGRS.2023.3258189.

[4] Z. Li, M. Zhang, K. Liang, and J. Wang, "Optical remote sensing image characteristics of large amplitude convex mode-2 internal solitary waves: An experimental study," *Acta Oceanologica Sinica*, vol. 42, no. 6, pp. 16–23, Aug. 2023, doi: 10.1007/s13131-022-2145-7.

[5] A. R. Osborne and T. L. Burch, "Internal solitons in the Andaman Sea," *Science*, vol. 208, no. 4443, pp. 451–460, May 1980, doi: 10.1126/science.208.4443.451.

[6] S. R. Ramp et al., "Internal solitons in the northeastern South China Sea part I: Sources and deep water propagation," *IEEE J. Ocean. Eng.*, vol. 29, no. 4, pp. 1157–1181, Oct. 2004, doi: 10.1109/JOE.2004.840839.

[7] M. H. Alford et al., "Speed and evolution of nonlinear internal waves transiting the South China Sea," *J. Phys. Oceanogr.*, vol. 40, no. 6, pp. 1338–1355, Jun. 2010, doi: 10.1175/2010JPO4388.1.

[8] X. Huang et al., "An extreme internal solitary wave event observed in the northern South China Sea," *Sci. Rep.*, vol. 6, Jul. 2016, Art. no. 30041, doi: 10.1038/srep30041.

[9] X. Huang et al., "Temporal variability of internal solitary waves in the northern South China Sea revealed by long-term mooring observations," *Prog. Oceanogr.*, vol. 201, Feb. 2022, Art. no. 102716, doi: 10.1016/j.pocean.2021.102716.

[10] Y. Yang et al., "Three-dimensional structures of internal solitary waves in the northern South China Sea revealed by mooring array observations," *Prog. Oceanogr.*, vol. 209, Dec. 2022, Art. no. 102907, doi: 10.1016/j.pocean.2022.102907.

[11] X. Bai, K. G. Lamb, Z. Liu, and J. Hu, "Intermittent generation of internal solitary-like waves on the northern shelf of the South China Sea," *Geophys. Res. Lett.*, vol. 50, no. 6, Mar. 2023, Art. no. e2022GL102502, doi: 10.1029/2022GL102502.

[12] Chonnaniyah, T. Osawa, A. R. As-Syakur, I. W. G. A. Karang, and J. C. B. da Silva, "On the distinction of seasonal internal solitary waves characteristics in the Lombok Strait based on multi-satellite data," *Int. J. Remote Sens.*, early access, doi: 10.1080/01431161.2023.2242592.

[13] R. E. Davis and A. Acrivos, "Solitary internal waves in deep water," *J. Fluid Mech.*, vol. 29, no. 3, pp. 593–607, 1967.

[14] Y. J. Yang, Y. C. Fang, T. Y. Tang, and S. R. Ramp, "Convex and concave types of second baroclinic mode internal solitary waves," *Nonlinear Processes Geophys.*, vol. 17, no. 6, pp. 605–614, 2010, doi: 10.5194/npg-17-605-2010.

[15] Y. J. Yang et al., "Observations of second baroclinic mode internal solitary waves on the continental slope of the northern South China Sea," *J. Geophys. Res. Oceans*, vol. 114, Oct. 2009, Art. no. C10003, doi: 10.1029/2009JC005318.

[16] S. R. Ramp, Y. J. Yang, D. B. Reeder, M. C. Buijsman, and F. L. Bahr, "The evolution of mode-2 nonlinear internal waves over the northern Heng-Chun Ridge south of Taiwan," *Nonlinear Processes Geophys.*, vol. 22, no. 4, pp. 413–431, 2015, doi: 10.5194/npg-22-413-2015.

[17] L. Chen et al., "Dynamic and statistical features of internal solitary waves on the continental slope in the northern South China Sea derived from mooring observations," *J. Geophys. Res. Oceans*, vol. 124, no. 6, pp. 4078–4097, Jun. 2019, doi: 10.1029/2018JC014843.

[18] L. Chen et al., "Mooring observed mode-2 internal solitary waves in the northern South China Sea," *Acta Oceanologica Sinica*, vol. 39, no. 11, pp. 44–51, Nov. 2020, doi: 10.1007/s13131-020-1667-0.

[19] L. Rong, X. Xiong, and L. Chen, "Assessment of KdV and eKdV theories for simulating internal solitary waves in the continental slope of the South China Sea," *Continental Shelf Res.*, vol. 256, Mar. 2023, Art. no. 104944, doi: 10.1016/j.csr.2023.104944.

[20] A. N. Serebryany and E. E. Khimchenko, "Internal waves of mode 2 in the Black Sea," *Doklady Earth Sci.*, vol. 488, no. 2, pp. 1227–1230, Oct. 2019, doi: 10.1134/S1028334X19100180.

[21] M. D. Rayson, N. L. Jones, and G. N. Ivey, "Observations of large-amplitude mode-2 nonlinear internal waves on the Australian north West shelf," *J. Phys. Oceanogr.*, vol. 49, no. 1, pp. 309–328, Jan. 2019, doi: 10.1175/JPO-D-18-0097.1.

[22] H. Qian, X. Huang, J. Tian, and W. Zhao, "Shoaling of the internal solitary waves over the continental shelf of the northern South China Sea (in Chinese)," *Acta Oceanologica Sinica*, vol. 34, no. 9, pp. 35–42, 2015, doi: 10.1007/s13131-015-0734-4.

[23] Z. Li et al., "Experimental study on optical imaging of convex mode-2 internal solitary waves in calm water," *IEEE Geosci. Remote Sens. Lett.*, vol. 20, Jun. 2023, Art. no. 6006205, doi: 10.1109/LGRS.2023.3281850.

[24] G. Sinnett et al., "Large-amplitude internal wave transformation into shallow water," *J. Phys. Oceanogr.*, vol. 52, no. 10, pp. 2539–2554, Oct. 2022, doi: 10.1175/JPO-D-21-0273.1.

[25] Y.-J. Yang, T. Y. Tang, M. H. Chang, A. K. Liu, M.-K. Hsu, and S. R. Ramp, "Solitons northeast of Tung-Sha Island during the ASIAEX pilot studies," *IEEE J. Ocean. Eng.*, vol. 29, no. 4, pp. 1182–1199, Oct. 2004, doi: 10.1109/JOE.2004.841424.

[26] D. Dong, X. Yang, X. Li, and Z. Li, "SAR observation of eddy-induced mode-2 internal solitary waves in the South China Sea," *IEEE Trans. Geosci. Remote Sens.*, vol. 54, no. 11, pp. 6674–6686, Nov. 2016, doi: 10.1109/TGRS.2016.2587752.
[27] C. Jackson, "Internal wave detection using the moderate resolution imaging spectroradiometer (MODIS)," *J. Geophys. Res. Oceans*, vol. 112, no. C11, Nov. 2007, Art. no. C11012, doi: 10.1029/2007JC004220.
[28] B. Liu, H. Yang, Z. Zhao, and X. Li, "Internal solitary wave propagation observed by tandem satellites," *Geophys. Res. Lett.*, vol. 41, no. 6, pp. 2077–2085, Mar. 2014, doi: 10.1002/2014GL059281.
[29] B. Liu and E. J. D'Sa, "Oceanic internal waves in the Sulu–Celebes Sea under sunglint and moonglint," *IEEE Trans. Geosci. Remote Sens.*, vol. 57, no. 8, pp. 6119–6129, Aug. 2019, doi: 10.1109/TGRS.2019.2904402.
[30] C. M. Tensubam, N. J. Raju, M. K. Dash, and H. Barskar, "Estimation of internal solitary wave propagation speed in the Andaman Sea using multi-satellite images," *Remote Sens. Environ.*, vol. 252, Jan. 2021, Art. no. 112123, doi: 10.1016/j.rse.2020.112123.
[31] J. Meng et al., "Remote sensing survey and research on internal solitary waves in the South China Sea-Western Pacific-East Indian Ocean (SCS-WPAC-EIND)," *Acta Oceanologica Sinica*, vol. 41, no. 10, pp. 154–170, Oct. 2022, doi: 10.1007/s13131-022-2018-0.
[32] X. Zhang and X. Li, "Satellite data-driven and knowledge-informed machine learning model for estimating global internal solitary wave speed," *Remote Sens. Environ.*, vol. 283, Oct. 2022, Art. no. 113328, doi: 10.1016/j.rse.2022.113328.
[33] C. Jackson, J. Da Silva, G. Jeans, W. Alpers, and M. Caruso, "Nonlinear internal waves in synthetic aperture radar imagery," *Oceanography*, vol. 26, no. 2, pp. 68–79, Jun. 2013, doi: 10.5670/oceanog.2013.32.
[34] C. Cox and W. Munk, "Measurement of the roughness of the sea surface from photographs of the sun's glitter," *J. Opt. Soc. Amer.*, vol. 44, no. 11, pp. 838–850, Nov. 1954, doi: 10.1364/JOSA.44.000838.
[35] C. Melsheimer and L. K. Kwoh, "Sun glitter in spot images and the visibility of oceanic phenomena," in *Proc. 22nd Asian Conf. Remote Sens.*, 2001, pp. 870–875.
[36] C. R. Jackson and W. Alpers, "The role of the critical angle in brightness reversals on sunglint images of the sea surface," *J. Geophys. Res. Oceans*, vol. 115, no. C9, Sep. 2010, Art. no. C09019, doi: 10.1029/2009JC006037.
[37] M. Zhang, J. Wang, X. Chen, Y. Mei, and X. Zhang, "An experimental study on the characteristic pattern of internal solitary waves in optical remote-sensing images," *Int. J. Remote Sens.*, vol. 40, no. 18, pp. 7017–7032, Sep. 2019, doi: 10.1080/01431161.2019.1597308.
[38] J. M. Magalhaes and J. C. B. da Silva, "Satellite altimetry observations of large-scale internal solitary waves," *IEEE Geosci. Remote Sens. Lett.*, vol. 14, no. 4, pp. 534–538, Apr. 2017, doi: 10.1109/LGRS.2017.2655621.
[39] J. M. Magalhaes et al., "Using a tandem flight configuration between Sentinel-6 and Jason-3 to compare SAR and conventional altimeters in sea surface signatures of internal solitary waves," *Remote Sens.*, vol. 15, no. 2, Jan. 2023, Art. no. 392, doi: 10.3390/rs15020392.
[40] X. Zhang and X. Li, "Unveiling three-dimensional sea surface signatures caused by internal solitary waves: Insights from the surface water ocean topography mission," *J. Oceanol. Limnol.*, early access, doi: 10.1007/s00343-024-3286-7.
[41] H. Qian, X. Huang, J. Tian, and W. Zhao, "Shoaling of the internal solitary waves over the continental shelf of the northern South China Sea," *Acta Oceanologica Sinica*, vol. 34, no. 9, pp. 35–42, Sep. 2015, doi: 10.1007/s13131-015-0734-4.
[42] C. R. de Macedo et al., "Spatial and temporal variability in mode-1 and mode-2 internal solitary waves from MODIS-Terra sun glint off the Amazon shelf," *Ocean Sci.*, vol. 19, no. 5, pp. 1357–1374, Sep. 2023, doi: 10.5194/os-19-1357-2023.
[43] M. Zhang, J. Wang, Z. Li, K. Liang, and X. Chen, "Laboratory study of the impact of the surface solitary saves created by the internal solitary waves on optical imaging," *IEEE J. Geophys. Res. Oceans*, vol. 127, no. 2, Feb. 2022, Art. no. e2021JC017800, doi: 10.1029/2021JC017800.
[44] M. Zhang et al., "Study on optical imaging signals of rough surfaces caused by ISWs in the ocean," *IEEE Trans. Geosci. Remote Sens.*, vol. 61, Jul. 2023, Art. no. 1000814, doi: 10.1109/TGRS.2023.3291727.
[45] W. Alpers, "Theory of radar imaging of internal waves," *Nature*, vol. 314, no. 21, pp. 245–247, Mar. 1985.
[46] L. Zou, Y. Hu, Z. Wang, Y. Pei, and Z. Yu, "Computational analyses of fully nonlinear interaction of an internal solitary wave and a free surface wave," *AIP Adv.*, vol. 9, no. 3, Mar. 2019, Art. no. 035234, doi: 10.1063/1.5088428.
[47] G. la Forgia and G. Sciortino, "The role of the free surface on interfacial solitary waves," *Phys. Fluids*, vol. 31, no. 10, Oct. 2019, Art. no. 106601, doi: 10.1063/1.5120621.
[48] Q. Zheng, Y. Yuan, V. Klemas, and X. Yan, "Theoretical expression for an ocean internal soliton synthetic aperture radar image and determination of the soliton characteristic half width," *J. Geophys. Res. Oceans*, vol. 106, no. C12, pp. 31415–31423, Dec. 2001, doi: 10.1029/2000JC000726.
[49] Z. Zhao, B. Liu, and X. Li, "Internal solitary waves in the China seas observed using satellite remote-sensing techniques: A review and perspectives," *Int. J. Remote Sens.*, vol. 35, no. 11-12, pp. 3926–3946, 2014, doi: 10.1080/01431161.2014.916442.
[50] A. K. Liu, F. Su, M. Hsu, N. Kuo, and C. Ho, "Generation and evolution of mode-two internal waves in the South China Sea," *Continental Shelf Res.*, vol. 59, pp. 18–27, May 2013, doi: 10.1016/j.csr.2013.02.009.
[51] D. Hong, C. Yang, and K. Ouchi, "Estimation of internal wave velocity in the shallow South China Sea using single and multiple satellite images," *Remote Sens. Lett.*, vol. 6, no. 6, pp. 448–457, Jun. 2015, doi: 10.1080/2150704X.2015.1034884.
[52] A. Brandt and K. R. Shipley, "Laboratory experiments on mass transport by large amplitude mode-2 internal solitary waves," *Phys. Fluids*, vol. 26, no. 4, Apr. 2014, Art. no. 046601, doi: 10.1063/1.4869101.
[53] V. Vlasenko, N. Stashchuk, C. Guo, and X. Chen, "Multimodal structure of baroclinic tides in the South China Sea," *Nonlinear Processes Geophys.*, vol. 17, no. 5, pp. 529–543, 2010, doi: 10.5194/npg-17-529-2010.
[54] S. R. Ramp, Y. J. Yang, D. B. Reeder, and F. L. Bahr, "Observations of a mode-2 nonlinear internal wave on the northern Heng-Chun Ridge south of Taiwan," *J. Geophys. Res. Oceans*, vol. 117, Mar. 2012, Art. no. C03043, doi: 10.1029/2011JC007662.
[55] T. Yan, Y. Qi, Z. Jing, and S. Cai, "Seasonal and spatial features of barotropic and baroclinic tides in the northwestern South China Sea," *J. Geophys. Res. Oceans*, vol. 125, no. 1, Jan. 2020, Art. no. e2018JC014860, doi: 10.1029/2018JC014860.
[56] X. Li, Z. Zhao, and W. G. Pichel, "Internal solitary waves in the northwestern South China Sea inferred from satellite images," *Geophys. Res. Lett.*, vol. 35, no. 13, Jul. 2008, Art. no. L13605, doi: 10.1029/2008GL034272.

Zhixin Li was born in Shandong, China, in 1996. He received the B.S. degree in physics from the School of Physics and Electronic Science, Shandong Normal University, Jinan, China, in 2019. He is currently working toward the Ph.D. degree in ocean technology with the School of Physics and Optoelectronic Engineering, Ocean University of China, Qingdao, China.

His research interests are internal wave experiments and optical remote sensing.

Jing Wang was born in Jiangsu, China, in 1962. She received the B.S. degree in physics from Inner Mongolia Normal University, Hohhot, China, in 1984, and the Ph.D. degree in ocean information detection and processing from the Ocean University of China, Qingdao, China, in 2008.

She is currently a Professor with the School of Physics and Optoelectronic Engineering, Ocean University of China. Her research interests include marine satellite remote sensing exploration, internal solitary waves, and fiber optic sensors.

Xu Chen received the B.S. degree in marine science and the M.S. and Ph.D. degrees in physical oceanography from the Ocean University of China, Qingdao, China, in 2001, 2003, and 2006, respectively.

He is currently a Professor with the Key Laboratory of Physical Oceanography, Ocean University of China, and also with the Qingdao National Laboratory for Marine Science and Technology, Qingdao, China. His research interests include internal waves and physical oceanography experiments.

Kexiao Lu was born in Shandong, China, in 1995. He received the M.E. degree in optical engineering in 2021 from the School of Physics and Optoelectronic Engineering, Ocean University of China, Qingdao, China, where he is currently working toward the Ph.D. degree in physical oceanography with the College of Oceanic and Atmospheric Sciences.

His research interests include satellite remote sensing and internal wave experiments.

Zhe Chang was born in Shandong, China, in 1998. He received the B.S. degree in optoelectronic information science and engineering in 2021 from the School of Information Science and Engineering, Ocean University of China, Qingdao, China, where he is currently working toward the master's degree in optical engineering with the School of Physics and Optoelectronic Engineering.

His research interests include internal wave experiments and optical remote sensing.

Yage Lu was born in Shandong, China, in 2000. He received the B.S. degree in mining engineering from the Shandong University of Science and Technology, Qingdao, China, in 2022. He is currently working toward the master's degree in optical engineering with the School of Physics and Optoelectronic Engineering, Ocean University of China, Qingdao, China.

His research interests include internal solitary waves, remote sensing, and machine learning.

Xiaochen Wang was born in Shandong, China, in 2000. He received the B.S. degree in optoelectronic information science and engineering from Wuhan Institute of Technology, Wuhan, China, in 2023. He is currently working toward the master's degree in optical engineering with the School of Physics and Optoelectronic Engineering, Ocean University of China, Qingdao, China.

His research interests include internal solitary waves, optical remote sensing, and machine learning.